Advanced Theory and Simulations

ADVANCED THEORY AND SIMULATIONS
www.advtheorysimul.com

RESEARCH ARTICLE OPEN ACCESS

Luminescence Spectra Simulation of Ce^{3+}-Activated Phosphors by Accumulating Emission Lines Along First-Principles Molecular Dynamics Trajectories

Satoru Matsuishi[1] | Hidekazu Ikeno[2] | Yukinori Koyama[3] | Takashi Takeda[4]

[1]Research Center For Materials Nanoarchitectonics, National Institute for Materials Science, Tsukuba, Ibaraki, Japan | [2]Department of Materials Science, Graduate School of Engineering, Osaka Metropolitan University, Sakai, Osaka, Japan | [3]Center for Basic Research On Materials, National Institute for Materials Science, Tsukuba, Ibaraki, Japan | [4]Research Center For Electronic and Optical Materials, National Institute for Materials Science, Tsukuba, Ibaraki, Japan

Correspondence: Satoru Matsuishi (matsuishi.satoru@nims.go.jp)

Received: 8 December 2025 | **Revised:** 24 April 2026 | **Accepted:** 18 May 2026

Keywords: Ce^{3+}-activated phosphor | first-principles molecular dynamics | photoluminescence

ABSTRACT

To simulate the luminescence emission spectra of Ce^{3+}-activated phosphors, we propose a method based on scalar-relativistic density functional theory with corrections for on-site Coulomb interactions, and first-principles molecular dynamics (FPMD) calculations, accounting for atomic thermal motion beyond harmonic oscillations. The FPMD calculations at finite temperature were performed with the excited-state (ES) electron configuration corresponding to the Ce $4f^05d^1$ state. Subsequently, the transition energies and probabilities of $4f^05d^1 \rightarrow 4f^15d^0$ transitions in each FPMD snapshot were calculated using the $N-1$ electron configuration in which the highest occupied level in the ground-state (GS) configuration is vacated. This is justified because applying Janak's theorem to a flat-band system allows each Kohn-Sham orbital's energy to be regarded as the total energy of an ES generated by an excitation from the highest level. The time-averaged spectrum was calculated by accumulating emission lines at the transition energies with amplitudes proportional to the probabilities. The spectra calculated for Ce^{3+}-activated yttrium aluminum garnet exhibit shapes and positions that resemble those measured at temperatures above 300 K. The peak energies and full widths at half maximum at 300 K for the series of Ce^{3+}-activated phosphors correlate with the experimental values, demonstrating the potential for predicting emission spectra of novel phosphors.

1 | Introduction

Researchers are currently searching for novel phosphors that exhibit stable emission brightness even at high operating temperatures in devices, as well as those that produce narrow-width single-line emission, for use in future high-brightness lighting [1–4] and 8K televisions defined by the BT.2020 standard [5], respectively. In the search for rare-earth-activated inorganic compounds that could serve as phosphors, data-driven and theory-driven methods, including machine learning (ML), are being used more and more employed [6–8]. The ML-based prediction of the spectral position and shape of emission bands in candidate compounds is expected to speed up the discovery of new materials. However, these properties vary based on the concentration of rare earth ions, impurities, defects, and measurement conditions, leading to a lack of consistent data for ML. Therefore, a method is required to determine the emission spectrum and its temperature dependence solely from the structural and compositional data of the host crystal and the information about the rare-earth dopants.

Since the electronic excitation and relaxation of rare-earth ions are understood as transitions among the multiplets of 4f and

5d electrons, their electronic states are calculated using methods that account for many-body effects of electrons, such as the state-averaged complete active space self-consistent field (SA-CASSCF) and second-order many-body perturbation theory (CASPT2) methods [9–12]. However, simulating electronic transition processes that involve dynamic changes in atomic positions is challenging with many-body techniques, which demand high computational costs. The Ce^{3+} ion is one such rare-earth ion, but it contains only one electron in its 4f shell. Therefore, its electronic state can be obtained even by a low-cost method based on density-functional theory (DFT), which does not consider many-body effects.

The delta self-consistent field (ΔSCF) approach using the constrained DFT (cDFT) technique is a DFT-based method previously used to estimate the spectral positions of absorption and emission maxima, i.e., peak energies, due to the $4f^1 5d^0 \rightarrow 4f^0 5d^1$ and $4f^0 5d^1 \rightarrow 4f^1 5d^0$ transitions [13, 14]. This method calculates the total energy difference between the ground-state electronic configuration (GSEC) and the excited-state electronic configuration (ESEC) to determine the absorption/emission peak energy. Additionally, by applying the quasi-1D harmonic oscillator model to the total energy change associated with the atomic configuration shift from a ground state (GS) relaxed to an excited state (ES) relaxed structure, it becomes possible to estimate the inhomogeneous broadening of the absorption and emission bands caused by phonon vibrations [15–17]. However, this approach only considers the total energy difference between specific electronic configurations and does not provide spectral details involving multiple optical transitions between various electronic configurations. Moreover, since atomic motion is approximated by a 1D harmonic oscillator, the influence of more complex higher-order harmonic vibrations and anharmonic motion on the emission energy and linewidth cannot be captured.

First-principles molecular dynamics (FPMD) using DFT electronic structure calculations can track the time evolution of atomic positions and momentum at finite temperature. By performing time-dependent density functional theory (TDDFT) calculations with the nonadiabatic couplings between wavefunctions at neighboring MD time steps, the electronic excitation and relaxation processes of Ce^{3+}-activated phosphors have been simulated [18, 19]. Therefore, FPMD allows the simulation of optical absorption and emission spectra while accounting for atomic motion. However, previous studies' FPMD and subsequent SCF calculations for emission spectral simulation were performed solely using GSEC, which is unsuitable for calculating emission spectra. The atomic motion before emission should be described using ESEC, and the electronic states obtained from GSEC do not include the electronic levels necessary for realistically representing emission spectra, as will be explained later.

In this paper, to obtain the emission spectra of Ce^{3+}-activated systems, we propose using FPMD calculations with ESEC and transition dipole moment (TDM) calculations with the N–1 electron configuration, which vacates the highest occupied level in GSEC. Applying Janak's theorem to the system in which the energy of each orbital is nearly independent of its occupancy, it can be shown that the energies of each one-electron level obtained from self-consistent field (SCF) calculations with the N–1 electron configuration approximate the total energies of the ground state and excited states generated by one-electron excitations from the ground state. Therefore, the results of the N–1 electron calculation are suitable for obtaining excitation and emission spectra due to one-electron transitions. By using the N–1 electron configuration, we obtained the electronic states of the Ce^{3+}-activated systems, which include multiple Ce 4f levels below the lowest Ce 5d level, leading to emission spectra consisting of multiple 5d→4f emission bands, as observed in the experimental spectra. By accumulating the emission lines located at transition energies with amplitudes proportional to the transition probabilities along the FPMD trajectory, we obtained an ensemble-averaged emission spectrum that accounts for the effects of atomic thermal motion at finite temperatures, without being restricted by the harmonic oscillator approximation. The spectral positions and shapes of the emission bands calculated for a Ce^{3+}-activated yttrium aluminum garnet (YAG) structural model between 100 and 700 K were compared with those of experimental spectra in the literature. Additionally, the emission peak energy and full width at half maximum (FWHM) at 300 K were calculated for a series of Ce^{3+}-activated systems and compared with literature values.

2 | Results and Discussion

2.1 | Calculation of Ce^{3+} $4f^1 5d^0 \leftrightarrow 4f^0 5d^1$ Transition Energies and Probabilities in a Fixed Configuration Coordinate

Figure 1a shows the energy level diagram of Ce^{3+} in the YAG crystal, based on experimental spectroscopic data [20]. Due to the spin-orbit (SO) interaction, the $4f^1 5d^0$ state splits into $^2F_{5/2}$ and $^2F_{7/2}$ multiplets with an energy difference of 0.290 eV (2340 cm^{-1}). The crystal field (CF) interaction further divides these multiplets into three and four substates, respectively. Meanwhile, the $4f^0 5d^1$ state splits into $5d_1$ and higher substates (such as $5d_2$, $5d_3$, etc.), mainly because of the CF interaction. The $^2F_{5/2}$ ground state is excited to the $5d_1$ and higher excited states (ESs) by blue to ultraviolet light, and these higher ESs quickly undergo a non-radiative transition to the $5d_1$ state. As a result, the radiative transition mainly occurs through $5d_1 \rightarrow {}^2F_{5/2}$ and $5d_1 \rightarrow {}^2F_{7/2}$ transitions.

A periodic structural model of Ce^{3+}-activated YAG crystal with the composition $CeY_{23}Al_{40}O_{96}$ was constructed by substituting a Y atom with Ce in the conventional face-centered cubic unit cell, which has a lattice parameter of approximately 12 Å. The ground-state relaxed configuration coordinate ($\mathbf{Q}_g$) was determined through DFT geometry optimization with a GSEC of 961 valence electrons (N = 961), where the Kohn-Sham orbitals (KSOs) are filled from lowest to highest energy. The KSO energy level diagram for the A_g state, generated using scalar-relativistic PBEsol+U calculations with GSEC and $U_{Ce}{}^{opt}$ = 4.68 eV, appears on the far left of Figure 1b. The level marker colors show whether the Ce 4f (blue), Ce 5d (red), or other atomic orbitals mainly contribute to each level. Between the valence band maximum (VBM), made up of oxygen 2p orbitals, and the lowest Ce 5d level just above the conduction band minimum (CBM), there is only one Ce 4f level with orbital index i = 1, which is the highest occupied level. The other unoccupied 4f levels are at least 4.1 eV

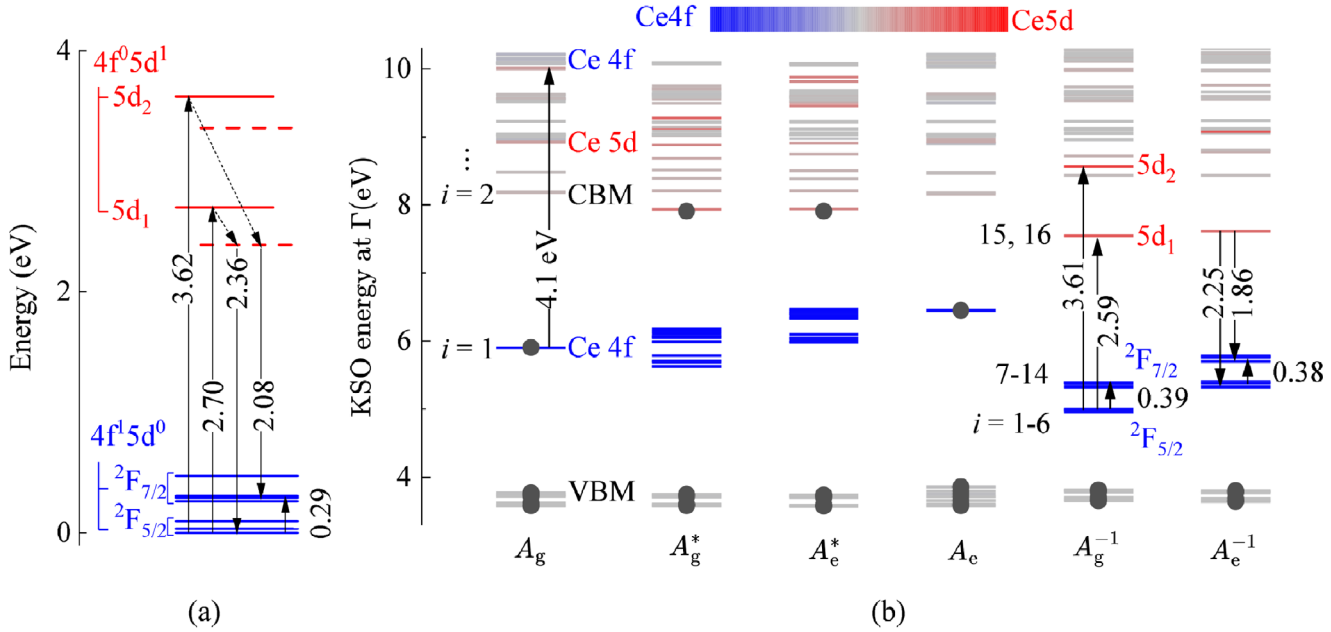

FIGURE 1 | (a) Multiplet energy diagram of Ce^{3+} in YAG. (b) One-electron Kohn-Sham orbital energy level diagrams for the $CeY_{23}Al_{40}O_{96}$ system, respectively calculated for the ground-state electron configuration (GSEC) in the GS-relaxed structure $\mathbf{Q}_g$ (A_g), the excited-state electron configuration (ESEC) in $\mathbf{Q}_g$ (A_g*), ESEC in the ES-relaxed structure $\mathbf{Q}_e$ (A_e*), GSEC in $\mathbf{Q}_e$ (A_e), the N–1 electron configuration in $\mathbf{Q}_g$ (A_g^{-1}), and the N–1 electron configuration in $\mathbf{Q}_e$ (A_e^{-1}). The level marker with a black spot indicates the occupied level, and the color of the marker indicates the contribution of atomic orbitals, with red and blue colors representing larger contributions of Ce 5d and Ce 4f orbitals, respectively.

higher than this occupied level. Therefore, when the occupied Ce 4f level is assigned to the 4f orbital occupied in the lowest substate of $^2F_{5/2}$ shown in Figure 1a, the energies of the other substates of $^2F_{5/2}$ and $^2F_{7/2}$, where one of the other 4f levels is occupied, are at least 4.1 eV higher than that of the lowest $^2F_{5/2}$ substate. This conflicts with the observation that the absorption due to 4f-4f transitions among the $^2F_{5/2}$ and $^2F_{7/2}$ substates occurs at an absorption energy below 0.5 eV. The presence of 4f-4f transitions will be discussed later.

Under the independent particle approximation, the TDM from the i-th orbital to the j-th orbital is described by Equation (1) using the wave functions φ_i and φ_j, and eigenvalues ϵ_i and ϵ_j in each state.

$$\boldsymbol{M}_{ij} = -\frac{i\hbar}{m_e\left(\epsilon_j - \epsilon_i\right)}\left\langle \varphi_i \middle| \boldsymbol{p} \middle| \varphi_j \right\rangle \tag{1}$$

where $\boldsymbol{p}$ is the momentum operator, and m_e is the rest mass of an electron. Then, the oscillator strength f_{ij} between the i-th and the j-th orbitals is given by Equation (2).

$$f_{ij} = \frac{2m_e\left(\epsilon_j - \epsilon_i\right)}{3\hbar^2}\left|M_{ij}\right|^2 \tag{2}$$

As shown by the red line in Figure 2a, the qualitative optical absorption spectrum of the Ag state in the visible to ultraviolet region was created by superimposing Gaussian peaks centered at $\epsilon_j - \epsilon_1$ with area intensities of $f_{1,j}$ ($j > 1$). The FWHM $w_{1,j}$ of all Gaussian peaks was fixed at 0.234 eV, a value estimated at 300 K using the ΔSCF approach described in the next section. The position and the height of the blue bar indicate the transition energy and oscillator strength of each transition, respectively. For comparison, the experimental fluorescence excitation spectrum at 300 K, as reported in the literature [21], is also shown as the dashed black line, rather than an absorption spectrum. In the experimental spectrum, two major peaks are observed at 2.70 eV, corresponding to the $^2F_{5/2}\rightarrow 5d_1$ transition, and at 3.62 eV, corresponding to the $^2F_{5/2}\rightarrow 5d_2$ transition. However, the lowest Ce 5d state is hybridized with delocalized Y 4d states that make up the CBM, and such peaks do not appear in the calculated spectrum. Similarly, the split fluorescence emission spectrum resulting from the coexistence of $5d_1\rightarrow{}^2F_{5/2}$ and $5d_1\rightarrow{}^2F_{7/2}$ transitions cannot be explained by the levels shown in this diagram, because 4f levels other than the lowest 4f level are located above the lowest 5d state.

In the ΔSCF approach, the absorption peak energy $\epsilon_{abs}^{\Delta SCF}$ for the $4f^15d^0\rightarrow 4f^05d^1$ transition is estimated as the total energy difference between the A_g state with GSEC and the A_g* state with ESEC in $\mathbf{Q}_g$, rather than the difference in one-electron level energy [13, 14]. In the A_g* state obtained by the cDFT calculation with ESEC, there are 14 unoccupied levels below the highest occupied level, as shown in the second diagram from the left in Figure 1b. The highest occupied level comprises Ce 5d orbitals, while the lower unoccupied levels mainly consist of Ce 4f orbitals. Similarly, the emission peak energy $\epsilon_{em}^{\Delta SCF}$ for the $4f^05d^1\rightarrow 4f^15d^0$ transition is estimated as the difference in total energy between the A_e* state with ESEC and the A_e state with GSEC in the ES-relaxed configuration coordinate $\mathbf{Q}_e$. This structure is determined by the cDFT structural optimization with the ESEC. From the obtained energy differences, $\epsilon_{abs}^{\Delta SCF}$, $\epsilon_{em}^{\Delta SCF}$ and the Stokes shift ΔS calculated as $\epsilon_{abs}^{\Delta SCF} - \epsilon_{em}^{\Delta SCF}$ were evaluated to be 2.75, 2.19, and 0.56 eV, respectively. These values are comparable to those of the experimental excitation and emission spectra, 2.70, 2.36, and 0.31 eV, respectively. In Figure 2a–c, the calculated absorption spectrum consists of a single Gaussian peak centered at $\epsilon_{abs}^{\Delta SCF}(0)$

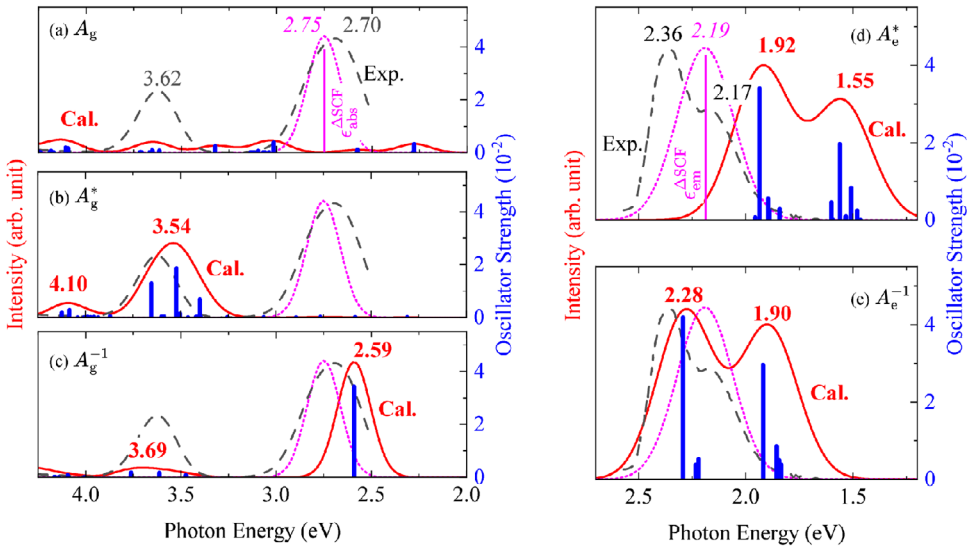

FIGURE 2 | Calculated absorption spectra (red curves) for YAG:Ce using TDM from the lowest Ce 4f level to higher levels in (a) A_g, (b) A_g*, and (c) A_g^{-1} states: Blue bars indicate the emission energies and the oscillator strengths; Black dashed lines shows the experimental luminescence excitation spectrum at 300 K for 2.31 eV emission taken from the literature, and the vertical magenta line indicates the ΔSCF absorption energy $\epsilon_{abs}^{\Delta SCF}$ at 0 K; Calculated luminescence emission spectra for YAG: Ce (red curve) using TDM from the lowest Ce 5d level to lower Ce 4f levels in (d) A_e* and (e) A_e^{-1} states. Black dashed lines show the experimental emission spectrum at 5 K for 2.75 eV excitation, and the magenta line indicates the ΔSCF emission energy $\epsilon_{em}^{\Delta SCF}(0)$ at 0 K.

with FWHM of $w_{abs}^{\Delta SCF}(300)$ is plotted as magenta dotted lines. The absorption peak at 2.75 eV overlapped with the $^2F_{5/2}\rightarrow 5d_1$ peak at 2.70 eV of the experimental spectrum. Since the ΔSCF scheme considers only GSEC corresponding to the lowest $^2F_{5/2}$ substate and ESEC corresponding to the $5d_1$ state, we cannot obtain information about other transitions such as $^2F_{5/2}\rightarrow 5d_2$ and $5d_1\rightarrow {}^2F_{7/2}$.

As shown in the second and third diagrams from the left in Figure 1b, the unoccupied 4f levels are positioned below the occupied Ce 5d level in the A_g* and A_e* states, as calculated with the ESEC configuration. By using $\epsilon_{j-}\ \epsilon_1$ and $f_{1,j}$ for $j >$ 1 obtained from the TDM calculation for the A_g* state, we can derive the absorption spectrum shown in Figure 2b, which features an absorption band peaking at 3.54 eV, consisting of three overlapping transition lines. However, this absorption energy exceeds the measured value by more than 0.8 eV, and the ΔSCF absorption energy $\epsilon_{abs}^{\Delta SCF}(0)$.

On the other hand, by using the transition energies $\epsilon_{15} - \epsilon_i$ and oscillator strength $f_{i,15}$ from the lowest occupied Ce 5d level (j = 15) to the unoccupied 4f levels (i = 1–14) in the A_e* state, we also obtain the emission spectrum as shown in Figure 2d. The FWHM $w_{i,15}$ of all transitions was set to 0.270 eV, a value estimated at 5 K using the ΔSCF approach described in the next section. For comparison, the measured spectrum at 5 K from literature [21] and the calculated spectrum with a single Gaussian peak at $\epsilon_{em}^{\Delta SCF}(0)$ = 2.19 eV are also plotted in this figure. Similar to the measured spectrum, which contains a peak at 2.36 eV corresponding to the $5d_1 \rightarrow {}^2F_{5/2}$ transition and a peak at 2.17 eV corresponding to the $5d_1 \rightarrow {}^2F_{7/2}$ transition, the spectrum of the A_e* state consists of two peaks at 1.92 and 1.55 eV. However, the peak positions deviate significantly from the experimental positions of 2.36 and 2.17 eV by −0.44 and −0.62 eV, respectively. This contrasts with the agreement of the $\epsilon_{em}^{\Delta SCF}(0)$ with the experimental $5d_1 \rightarrow {}^2F_{5/2}$ energy to within 0.17 eV.

Here, we demonstrate that SCF calculations using the N−1 electron configuration, which vacates the highest occupied orbital in GSEC, as shown in the fifth diagram from the left in Figure 1b, produce electronic states that are more suitable for obtaining the absorption and emission spectra. According to Janak's theorem [22], which describes the relationship between one-electron orbital energy and total energy in DFT, the energy ϵ_i of the i-th band is equal to the total energy E_{tot} partially differentiated with respect to the occupation number n_i of the i-th orbital.

$$\epsilon_i = \frac{\partial E_{tot}}{\partial n_i} \tag{3}$$

Therefore, in the A^{-1} state with an N−1 electron configuration corresponding to the Ce $4f^05d^0$ state and a total energy of $E_{tot}[4f^05f^0]$, the one-electron energy of the lowest Ce 4f band ϵ_{4f} is expressed by

$$\epsilon_{4f} = \lim_{\delta\to 0} \frac{E_{tot}\left[4f^{\delta}5d^0\right] - E_{tot}\left[4f^05d^0\right]}{\delta} \tag{4}$$

Assuming the flat band where the total energy is proportional to the 4f band occupancy, Equation (4) is approximated by

$$\epsilon_{4f} \sim \lim_{\delta\to 0} \frac{E_{tot}\left[4f^15d^0\right]\delta + E_{tot}\left[4f^05d^0\right](1-\delta) - E_{tot}\left[4f^05d^0\right]}{\delta} \tag{5}$$

$$\sim E_{tot}\left[4f^15d^0\right] - E_{tot}\left[4f^05d^0\right]$$

Similarly, the one-electron energy of the lowest Ce 5d band ϵ_{5d} is given by

$$\epsilon_{5d} = \lim_{\delta \to 0} \frac{E_{tot}\left[4f^0 5d^\delta\right] - E_{tot}\left[4f^0 5d^0\right]}{\delta} \sim E_{tot}\left[4f^0 5d^1\right] - E_{tot}\left[4f^0 5d^0\right] \quad (6)$$

Then, the difference between the one-electron energies is estimated by

$$\epsilon_{5d} - \epsilon_{4f} \sim E_{tot}\left[4f^0 5d^1\right] - E_{tot}\left[4f^1 5d^0\right] \quad (7)$$

This equals the transition energy from the A state with GSEC ($4f^1 5d^0$) to the A^* state with ESEC ($4f^0 5d^1$). The same concept applies to any single-electron excitation and relaxation between the i-th and j-th bands in the A^{-1} state, where the orbital index for the highest occupied band with GSEC is 1. Each one-electron level corresponds to either the multielectron ground state (GS) ($i = 1$) or the multielectron excited state (ES) ($i > 1$) resulting from a single-electron excitation from the ground state. For comparison, ϵ_{4f}, ϵ_{5d}, and $\epsilon_{5d} - \epsilon_{4f}$ were approximated by

$$\epsilon_{4f} \sim E_{tot}\left[4f^1 5d^0\right] - E_{tot}\left[4f^0 5d^0\right], \quad \epsilon_{5d} \sim E_{tot}\left[4f^1 5d^1\right] - E_{tot}\left[4f^1 5d^0\right] \quad (8)$$

$$\epsilon_{5d} - \epsilon_{4f} \sim E_{tot}\left[4f^1 5d^1\right] + E_{tot}\left[4f^0 5d^0\right] - 2E_{tot}\left[4f^1 5d^0\right]$$

in the A state with GSEC ($4f^1 5d^0$) and

$$\epsilon_{4f} \sim E_{tot}\left[4f^1 5d^1\right] - E_{tot}\left[4f^0 5d^1\right], \quad \epsilon_{5d} \sim E_{tot}\left[4f^0 5d^1\right] - E_{tot}\left[4f^0 5d^0\right] \quad (9)$$

$$\epsilon_{5d} - \epsilon_{4f} \sim 2E_{tot}\left[4f^0 5d^1\right] - E_{tot}\left[4f^0 5d^0\right] - E_{tot}\left[4f^1 5d^1\right]$$

in the A^* state with ESEC ($4f^0 5d^1$). The $\epsilon_{5d} - \epsilon_{4f}$ in A and A^* states have no direct relationship with the transition energy from the A state to the A^* state. Therefore, the eigenvalues and wavefunctions in A^{-1} are the most suitable for approximately calculating the transition energies and probabilities between many-electron states.

The energy level diagram of the $A_g{}^{-1}$ state, obtained through the $N-1$ electron calculation for $\mathbf{Q}_g$, is shown in the fifth column from the left of Figure 1b. Corresponding to the Ce $4f^0 5d^0$ state, all Ce 4f and 5d levels become empty with orbital indices from 1 to 16, including the lowest 4f level. Seven doubly degenerate levels, consisting of Ce 4f orbitals, are located 2.25 to 2.62 eV below the lowest level composed of Ce 5d orbitals. Similar to the $^2F_{5/2}$ and $^2F_{7/2}$ states in Figure 1a, these levels are divided into three lower and four higher levels, with a centroid separation of 0.37 eV. Using $\epsilon_j - \epsilon_1$ and $f_{1,j}$ ($j > 3$) obtained from TDM calculation for $A_g{}^{-1}$, an absorption spectrum in the visible to ultraviolet range was calculated with prominent peaks at 2.59 and 3.69 eV due to 4f-5d transitions, as shown in Figure 2c. This spectrum resembles the experimental excitation spectrum with peaks at 2.70 and 3.62 eV. Furthermore, as shown in Figure S1, an infrared absorption spectrum with weak peaks due to 4f-4f transitions below 0.43 eV was also calculated, consistent with the experimental spectrum reported in the literature.

By performing the $N-1$ electron calculation for $\mathbf{Q}_e$, we obtained the energy level diagram for the $A_e{}^{-1}$ state shown on the far right of Figure 1b. Table 1 lists the energy ϵ_i of the Ce 4f levels and the lowest 5d levels with indices i from 1 to 16, relative to the energy of the lowest unoccupied orbitals ($i = 1, 2$) in the diagram. Each odd-numbered orbital with index $i = 1, 3, \ldots, 13$ degenerates with the even-numbered orbital with index $i + 1$. For comparison, the experimental multiplet energies of Ce^{3+} in YAG, $\epsilon_{n\Gamma_5}$ ($n = 1, 2, \ldots, 8$) based on the results of the CF theory fitting of the infrared absorption data and the luminescence measurement are listed in Table 1 [20]. Additionally, the theoretical literature values of $\epsilon_{n\Gamma_5}$ are also listed. These were calculated using the SA-CASSCF and CASPT2 methods with a $(CeO_8)^{13-}$ embedded cluster model in the GS-relaxed structure, while considering many-body effects [12]. Each degenerated one-electron level corresponds to a sublevel of the multiplet, $1\Gamma_5$-$3\Gamma_5$ of $^2F_{5/2}$, $4\Gamma_5$-$7\Gamma_5$ of $^2F_{7/2}$, and $8\Gamma_5$ of $5d_1$. The separation between the centroids of levels $i = 1$–6 and levels $i = 7$–14, corresponding to the SO splitting of $^2F_{5/2}$ and $^2F_{7/2}$ is overestimated at 2858 cm^{-1}. This value is 1.22 times greater than the experimental value of 2334 cm^{-1} and 1.12 times greater than the SA-CASSCF/CASPT2 calculation value of 2543 cm^{-1}. The possible causes of the overestimation are the neglect of the multi-electron effect and the error in estimating the SO interaction in the PAW method, which depends on the selection of the exchange-correlation functional [23].

Table 1 also shows the oscillator strengths $f_{i,15}$ ($i = 1$–14) between Ce 4f levels and the lowest Ce 5d level obtained from TDM calculations, as well as the sum of those from degenerate levels $f_{i,15} + f_{i+1,15}$ ($i = 1, 3, \ldots, 13$). For comparison, the table also lists the oscillator strengths $f_{n\Gamma_5,8\Gamma_5}$ between $^2F_{5/2}$ and $^2F_{5/2}$ substates and $5d_1$ state calculated using the SA-CASSCF and CASPT2 methods in a past paper [12]. Each $f_{i,15} + f_{i+1,15}$ has the same magnitude as the $f_{n\Gamma_5,8\Gamma_5}$ with $n = i$, indicating that the KSOs in the $A_e{}^{-1}$ state inherit the character of the corresponding GS and ES multi-electron orbitals. Furthermore, the ratio of $\sum_{i=7}^{14} f_{i,15} / \sum_{i=1}^{6} f_{i,15}$ corresponding to the intensity ratio of $5d_1 \rightarrow {}^2F_{5/2}$ and $5d_1 \rightarrow {}^2F_{7/2}$ emissions is 0.90, which is also comparable to $\sum_{n=4}^{7} f_{n\Gamma_5,8\Gamma_5} / \sum_{n=1}^{3} f_{n\Gamma_5,8\Gamma_5} = 0.81$ of SA-CASSCF calculation.

As shown in Figure 2e, the emission spectrum features two peaks at 2.28 and 1.90 eV, which are obtained using $\epsilon_{15} - \epsilon_i$ and $f_{i,15}$ ($i = 1$–14) in the $A_e{}^{-1}$ state in Table 1. The deviations of the peak energies from the experimental values are −0.06 and −0.27 eV, respectively, indicating better agreement with the experimental data compared to results for the $A_e{}^*$ state. Furthermore, the deviation of the higher peak energy from $\epsilon_{em}^{\Delta SCF}(0)$ also decreases from 0.27 to −0.09 eV, which further improves the consistency with the result obtained by the ΔSCF method. From the results of TDM calculations of $A_g{}^{-1}$ and $A_e{}^{-1}$ states, the peak energies of the lowest $4f^1 5d^0 \rightarrow 4f^0 5d^1$ absorption and the highest $4f^0 5d^1 \rightarrow 4f^1 5d^0$ emission are estimated to be 2.59 and 2.28 eV, respectively. Thus, the Stokes shift is evaluated to be 0.31 eV, which almost agrees with the experimental value of 0.34 eV.

TABLE 1 | Relative energies of Ce 4f (i = 1–14) and Ce 5d (i = 15,16) KSO levels (ϵ_i, cm^{-1}), oscillator strengths of 4f→5d transitions ($f_{i,15}$) and sum oscillator strength of degenerated transitions ($f_{i,15} + f_{i+1,15}$) from N–1 electron calculation for ES-relaxed structure of YAG:Ce structure model. Experimental multi-electron orbital energies ($\epsilon^{exp}_{n\Gamma5}$, cm^{-1}) of $^2F_{5/2}$, $^2F_{7/2}$, and $^2D_{3/2}$ multiplet terms measured by CF theory fitting for IR absorption data and theoretical orbital energies ($\epsilon^{cal}_{n\Gamma5}$, cm^{-1}) with oscillator strengths ($f^{cal}_{n\Gamma5,8\Gamma5}$) obtained by SA-CASSCF calculation are also listed.

i	ϵ_i	$f_{i,15}$	$f_{i,15} + f_{i+1,15}$	n	$\epsilon^{exp}_{n\Gamma_5}$	$\epsilon^{cal}_{n\Gamma_5}$	$f^{cal}_{n\Gamma_5,8\Gamma_5}$	Term
1	0	2.3×10^{-2}	4.2×10^{-2}	1	0	0	3.2×10^{-2}	$^2F_{5/2}$
2		1.9×10^{-2}						
3	486	2.1×10^{-3}	3.9×10^{-3}	2	273	430	3.3×10^{-3}	
4		1.8×10^{-3}						
5	586	1.8×10^{-3}	5.2×10^{-3}	3	786	770	1.1×10^{-2}	
6		3.5×10^{-3}						
7	3018	5.2×10^{-3}	2.9×10^{-2}	4	2097	2260	2.5×10^{-2}	$^2F_{7/2}$
8		2.4×10^{-2}						
9	3518	2.4×10^{-3}	8.6×10^{-3}	5	2343	2500	9.9×10^{-3}	
10		6.3×10^{-3}						
11	3615	3.8×10^{-3}	4.9×10^{-3}	6	2485	2780	2.0×10^{-3}	
12		1.2×10^{-3}						
13	3648	2.9×10^{-3}	3.8×10^{-3}	7	3822	4230	7.8×10^{-4}	
14		8.9×10^{-4}						
15	18493	—	—	8	19 275	18 700	—	$^2D_{3/2}$ ($5d_1$)
16		—						

Using the TDM for $A_e{}^{-1}$ as defined in Equation (1), Einstein's A coefficient A_{ji}, which represents the probability of transition from the j-th level to the i-th level due to spontaneous photon emission, is given by Equation (10).

$$A_{ji} = \frac{e^3\left(\epsilon_j - \epsilon_i\right)^3}{3\pi\varepsilon_0\hbar^3c^3}\left|M_{ij}\right|^2 \tag{10}$$

The number of photons emitted per unit time is given by $A_{ji}\rho_j$, which is the product of A_{ji} and the occupancy ρ_j of the j-th level. If the transitions from the lowest Ce 5d level (j = 15) to the Ce 4f levels (i = 1–6 and 7–14) are the dominant radiative processes, then the reciprocal of the radiative transition time τ_r is given by the sum of $A_{15,i}$ for i = 1–14:

$$\tau_r{}^{-1} = \sum_{i=1}^{14} A_{15,i} \tag{11}$$

The τ_r is estimated to be 53 ns, which closely matches the experimental value of approximately 60 ns at low temperatures below 300 K, where radiative transitions dominate non-radiative transitions [21, 24].

As described above, using one-electron wavefunctions obtained through DFT calculations with the N–1 electron configuration enables the calculation of transition energies and TDMs for the $4f^15d^0 \rightarrow 4f^05d^1$ excitation and the $4f^05d^1 \rightarrow 4f^15d^0$ emission lines. This approach aligns with the results from photoluminescence excitation and emission spectra measurements, high-precision calculations considering multi-electron configurations, and the ΔSCF method.

Here, it is noted that TDM calculations using the N–1 electron configuration are only valid for systems such as Ce^{3+}-activated phosphors, where the energies of each KSO are hardly dependent on the occupied states and can be treated as a one-electron system. In other words, this method is not suitable for describing the excited states of systems that contain strongly correlated multiple 4f electrons, such as Eu^{2+} and other rare-earth activated phosphors.

2.2 | Ce^{3+} $4f^05d^1 \rightarrow 4f^15d^0$ Emission Spectrum Simulation Considering the Effect of Atomic Thermal Motion

In FPMD calculations, interatomic forces at time t are calculated using quantum mechanics of the electron system on fixed atomic coordinates. Using the atomic coordinates, velocities, and the calculated interatomic forces at time t, a classical mechanics calculation of the atoms over the time interval Δt was performed to find the coordinates and velocities at time $t + \Delta t$. FPMD does not consider the quantum mechanical motion of atoms, such as zero-point motion of harmonic oscillators, and therefore cannot precisely simulate atomic motion at low temperatures. Meanwhile, FPMD monitors the time evolution of configuration coordinates, capturing not only harmonic vibrational modes but also all atomic displacement modes accessible through thermal motion. This allows for the consideration of anharmonic motions that become important at high temperatures.

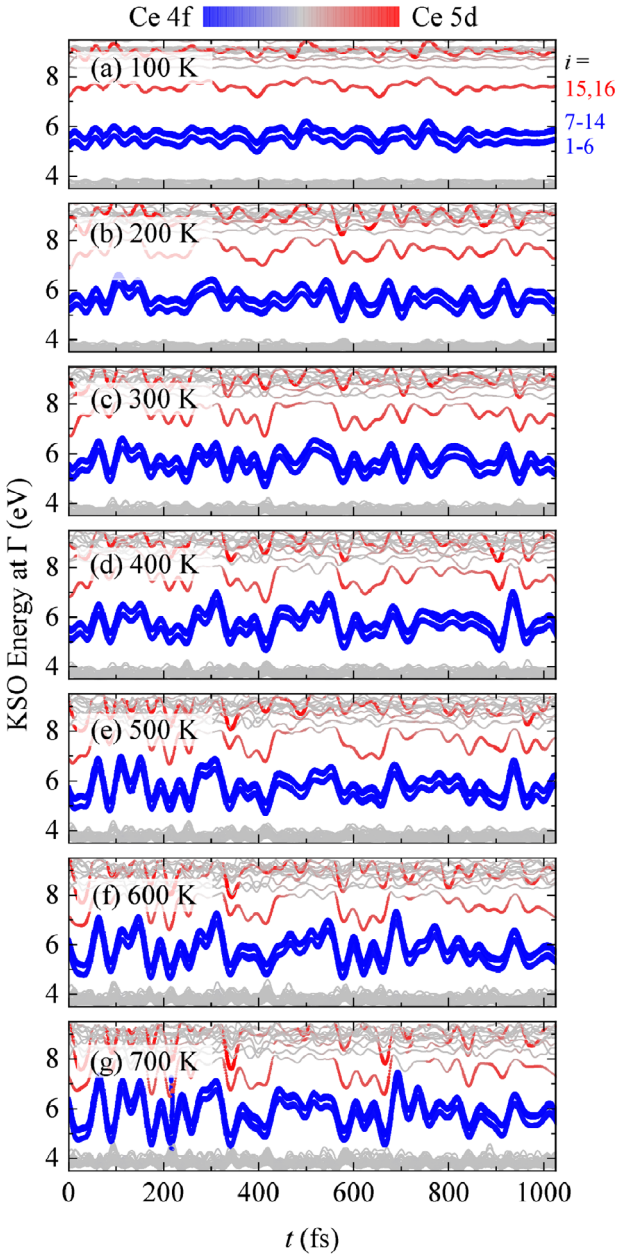

FIGURE 3 | Time evolution of KSO energies calculated for N–1 electron system on the trajectory of FPMD performed for YAG:Ce structure model with ESEC corresponding to $4f^0 5d^1$ state of Ce^{3+} ion at a temperature of (a) 100 K, (b) 200 K, (c) 300 K, (d) 400 K, (e) 500 K, (f) 600 K, and (g) 700 K. The line's color indicates the contribution of Ce 4f and 5d orbitals.

For the YAG:Ce model, MD calculations were performed using ESEC across a temperature range of 100–700 K. Figure 3 shows the time evolution of the KSO energies at the Γ point based on scalar relativistic SCF calculations using the N–1 electron configuration at each snapshot of the MD trajectory. The energies of the Ce 4f levels (i = 1, 2, …, 14), which are 1 to 2 eV above the VBM, and the Ce 5d levels (i = 15, 16), located 1 to 2 eV below the CBM, fluctuate periodically and vary over time. Their oscillation amplitudes increase with temperature.

As previously noted, transitions from orbital j = 15 to orbitals i = 1–6 (15→1-6) and 7–14 (15→7-14) correspond to $5d_1 \rightarrow {}^2F_{5/2}$ and $5d_1 \rightarrow {}^2F_{7/2}$ transitions in the multiplet energy diagram. Figure S2 shows how the mean radiative lifetime $\langle\tau_r\rangle$ depends on temperature. This lifetime is obtained as the reciprocal of the mean radiative transition rate, which is the average of τ_r calculated using Equation (11) at each snapshot of the MD trajectory.

$$\langle\tau_r\rangle^{-1} = \frac{1}{T}\int_0^T \sum_{i=1}^{14} A_{15,i}(t)\,dt \tag{12}$$

The calculated $\langle\tau_r\rangle^{-1}$ increases linearly with temperature, ranging from 56 ns at 100 K to 93 ns at 700 K. Values below 400 K closely match the experimentally observed luminescence lifetime [24]. Below 400 K, the experimental non-radiative relaxation rate is less than 10^6 s^{-1}, which is negligible compared to the experimental radiative relaxation rate, which is higher than 10^7 s^{-1} [24]. The homogeneous linewidth estimated from the lifetime ranges from 4.4×10^{-8} to 7.5×10^{-8} eV, which is negligible compared to the inhomogeneous linewidth caused by atomic motion.

A typical fluorescence spectrophotometer detects the radiation energy, which is the product of the number of photons and the photon energy, at each wavelength. Consequently, the theoretical time-averaged emission spectrum $I(\epsilon)$, which can be compared to the measured one, is expressed by Equation (13) as the sum of emission lines located at $\epsilon_{15} - \epsilon_i$ with the amplitude of $A_{15,i}\rho_{15}(\epsilon_{15} - \epsilon_i)$.

$$I(\epsilon) = \frac{1}{T}\int_0^T \sum_{i=1}^{14} A_{15,i}(t)\,\rho_{15}(t)\{\epsilon_{15}(t) - \epsilon_i(t)\} \times \delta\{\epsilon - \epsilon_{15}(t) + \epsilon_i(t)\}\,dt \tag{13}$$

If the occupancy of the lowest Ce 5d orbital $\rho_{15}(t)$ remains constant due to continuous excitations, Equation (13) is rewritten to

$$I(\epsilon) = \frac{1}{T}\int_0^T \sum_{i=1}^{14} A_{15,i}(t)\{\epsilon_{15}(t) - \epsilon_i(t)\}\,\delta\{\epsilon - \epsilon_{15}(t) + \epsilon_i(t)\}\,dt \tag{14}$$

As shown in Table 1, the energy differences between the 4f sublevels with orbital indices i from 1 to 6 or from 7 to 14, which correspond to ${}^2F_{5/2}$ or ${}^2F_{7/2}$ states, are less than 0.1 eV. This value is smaller than the FWHM of each 15→i emission line caused by atomic motions estimated by the ΔSCF method (>0.3 eV). Therefore, the six emission lines due to $5d_1 \rightarrow {}^2F_{5/2}$ transitions and the eight lines due to $5d_1 \rightarrow {}^2F_{7/2}$ transitions are each combined into a single emission band. To evaluate the FWHM induced by thermal atomic motion, the spectra of emission bands for the $5d_1 \rightarrow {}^2F_{5/2}$ and $5d_1 \rightarrow {}^2F_{7/2}$ components were counted separately using Equations (15) and (16).

$$I_{5/2}(\epsilon) = \frac{1}{T}\int_0^T \sum_{i=1}^{6} A_{15,i}(t)\{\epsilon_{15}(t) - \epsilon_i(t)\} \times \delta\{\epsilon - \epsilon_{15}(t) + \epsilon_i(t)\}\,dt \tag{15}$$

$$I_{7/2}(\epsilon) = \frac{1}{T}\int_0^T \sum_{i=7}^{14} A_{15,i}(t)\{\epsilon_{15}(t) - \epsilon_i(t)\} \times \delta\{\epsilon - \epsilon_{15}(t) + \epsilon_i(t)\}\, dt \quad (16)$$

Therefore, the overall spectrum averaged over time is found by adding these spectra.

$$I(\epsilon) = I_{5/2}(\epsilon) + I_{7/2}(\epsilon) \quad (17)$$

Figure 4 displays the stacked bar chart for $I_{5/2}(\epsilon)$ and $I_{7/2}(\epsilon)$ from 100 to 700 K, obtained using the emission lines accumulation (ELA) method. It is represented as histograms of $\epsilon_{15} - \epsilon_i$ weighted by $A_{15,i}(\epsilon_{15} - \epsilon_i)$ with a bin size of 0.01 eV. As shown by the 100 K data, $I_{5/2}(\epsilon)$ and $I_{7/2}(\epsilon)$ consist of single Gaussian peaks centered at $\epsilon_{5/2\text{cal}}$ and $\epsilon^{\text{cal}}_{7/2}$, respectively, with almost equal FWHMs $w^{\text{cal}}_{5/2}$ and $w^{\text{cal}}_{7/2}$. Below 200 K, the FWHM is smaller than the peak separation due to SO interaction, $\Delta^{\text{cal}}_{\text{SO}} = \epsilon^{\text{cal}}_{5/2} - \epsilon^{\text{cal}}_{7/2} \sim 0.38$ eV, so the presence of two peaks is recognized even in the whole spectrum $I(\epsilon)$. By fitting two Gaussian functions to $I_{5/2}(\epsilon)$ and $I_{7/2}(\epsilon)$, respectively, the transition energies at emission maxima $\epsilon^{\text{cal}}_{5/2}$ and $\epsilon^{\text{cal}}_{7/2}$, the FWHM $w^{\text{cal}}_{\text{em}} = (w^{\text{cal}}_{5/2} + w^{\text{cal}}_{7/2})/2$, and the area intensity ratio of the two spectral components $s^{\text{cal}}_{7/2}/s^{\text{cal}}_{5/2}$ were obtained as a function of temperature as shown in Figure 5a–c. For comparison, the experimental peak energies $\epsilon^{\text{exp}}_{5/2}$ and $\epsilon^{\text{exp}}_{7/2}$, FWHM $w^{\text{exp}}_{\text{em}} = (w^{\text{exp}}_{5/2} + w^{\text{exp}}_{7/2})/2$, and ratio $s^{\text{exp}}_{5/2}/s^{\text{exp}}_{7/2}$ were also plotted in Figure 5a–c. The experimental values were evaluated by fitting the peak functions to the measured spectra reported in the literature [21], as shown in Figure S3.

In Figure 5a, the peak energy $\epsilon^{\text{cal}}_{5/2}$ shifts from $\epsilon^{\text{cal}}_{5/2}(0) = 2.29(2)$ eV to lower energies with increasing temperature, exhibiting a temperature coefficient $d\epsilon^{\text{cal}}_{5/2}/dT$ of $-2.6(4) \times 10^{-4}$ eV/K (The number in parentheses indicates the standard deviation). The experimental peak energy $\epsilon^{\text{exp}}_{5/2}$ also shifts to lower energy from $\epsilon^{\text{exp}}_{5/2}(0) = 2.361(1)$ eV with a temperature coefficient $d\epsilon^{\text{exp}}_{5/2}/dT$ of $-1.8(6) \times 10^{-5}$ eV/K. In previous studies, the temperature dependence of emission peak energy was estimated by applying the quasi-1D harmonic oscillator model to potential energy surfaces in the configuration coordinate diagram obtained by ΔSCF approach, as shown in Figure S4 [15–17]. The Franck–Condon energy shifts from A_g to A_e states ($E^{\Delta\text{SCF}}_{\text{FC,g}}$) and from A_e* to A_g* states ($E^{\Delta\text{SCF}}_{\text{FC,e}}$) are evaluated by the ΔSCF approach to be 0.347 and 0.210 eV, respectively. On the other hand, the total normal coordinate change ΔQ from $\mathbf{Q}_g$ to $\mathbf{Q}_e$ defined by Equation (18) was evaluated to be 1.423 amu$^{1/2}$·Å.

$$\Delta Q = \sqrt{\sum_{\alpha\xi} m_\alpha \left(r_{e;\alpha\xi} - r_{g;\alpha\xi}\right)^2} \quad (18)$$

where α (= 1, 2, …) and ($\xi = x, y, z$) label atoms in the unit cell and coordinate in Cartesian axes, respectively, m_α represents atomic mass, and $r_{e;\alpha\xi}$ and $r_{g;\alpha\xi}$ are atomic coordinates in $\mathbf{Q}_e$ and $\mathbf{Q}_g$, respectively. Using the values of $E^{\Delta\text{SCF}}_{\text{FC,g}}$, $E^{\Delta\text{SCF}}_{\text{FC,e}}$, and ΔQ, the associated effective vibrational energies, $\Omega_g = (2E^{\Delta\text{SCF}}_{\text{FC,g}})^{1/2}/\Delta Q$ and $\Omega_e = (2E^{\Delta\text{SCF}}_{\text{FC,e}})^{1/2}/\Delta Q$, and the Huang-Rhys parameters, $S_g = E^{\Delta\text{SCF}}_{\text{FC,g}} / \hbar\Omega_g$ and $S_e = E^{\Delta\text{SCF}}_{\text{FC,e}} / \hbar\Omega_e$ for the A and the A* states are given as 37.8 meV and 29.4 meV, and 9.17 and 7.13, respectively. Then,

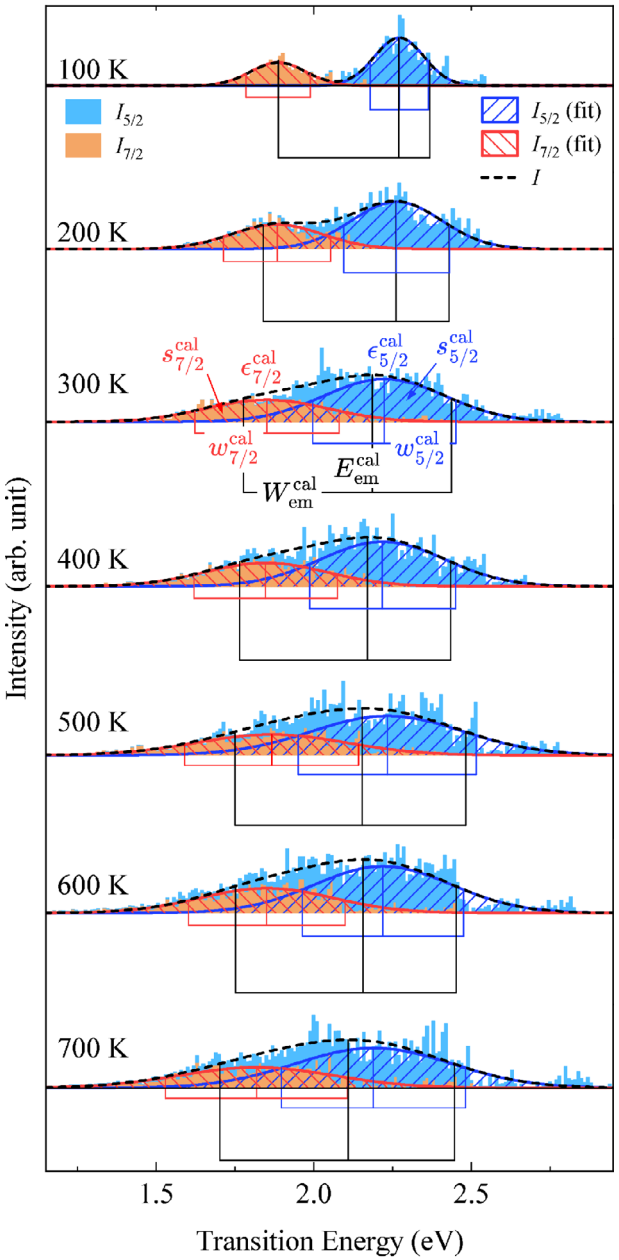

FIGURE 4 | Ce $4f^0 5d^1 \rightarrow 4f^1 5d^0$ emission spectra calculated by ELA method for YAG:Ce structure model at 100–700 K. Light blue and orange parts of stacked bar graphs respectively indicate intensities of $5d_1 \rightarrow {}^2F_{5/2}$ ($I_{5/2}(\epsilon)$) and the $5d_1 \rightarrow {}^2F_{7/2}$ ($I_{7/2}(\epsilon)$) components. Blue and red lines indicate peak fitting curves for $I_{5/2}(\epsilon)$ and $I_{7/2}(\epsilon)$ components, respectively, and the black dashed line indicates the sum of fitting curves.

the temperature dependence of the emission peak energy $\epsilon^{\Delta\text{SCF}}_{\text{em}}$ is obtained by using Equation (19) [15–17].

$$\epsilon_{\text{em}}(T) = \epsilon_{\text{em}}(0) + \left(\frac{\Omega_g^2 - \Omega_e^2}{\Omega_e^2} + \frac{8\Omega_g^4}{\Omega_e^2\left(\Omega_g^2 + \Omega_e^2\right)}\frac{\Delta S(0)}{\epsilon_{\text{em}}(0)}\right) k_B T \quad (19)$$

The magenta line in Figure 5a shows the temperature dependence of $\epsilon^{\Delta\text{SCF}}_{\text{em}}$ with $\epsilon^{\Delta\text{SCF}}_{\text{em}}(0) = 2.19$ eV and a temperature coefficient

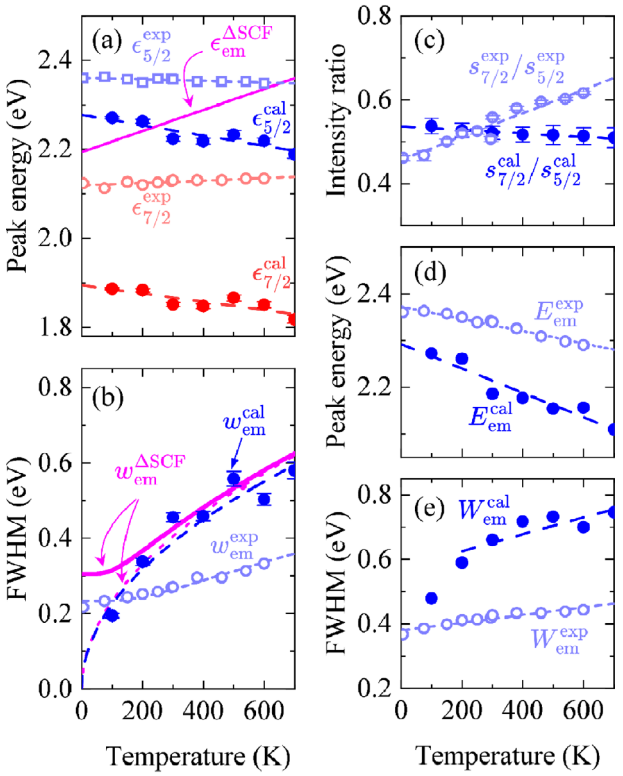

FIGURE 5 | Temperature dependences of peak profile parameters of the emission spectra calculated by the ELA method for YAG:Ce structure model: Peak energies $\epsilon^{cal}_{5/2}$ and $\epsilon^{cal}_{7/2}$(a), FWHM $w^{cal}_{em} = (w^{cal}_{5/2} + w^{cal}_{7/2})$ /2 (b), and areal intensity ratio $s^{cal}_{7/2}/s^{cal}_{5/2}$ (c) of $5d_1 \rightarrow {}^2F_{5/2}$ and $5d_1 \rightarrow {}^2F_{7/2}$ peaks, and peak energy E^{cal}_{em} (d) and FHWM W^{cal}_{em} of the whole emission band. For comparison, the parameters, $\epsilon^{exp}_{5/2}$ and $\epsilon^{exp}_{7/2}$, w^{exp}_{em}, $s^{exp}_{7/2}/s^{exp}_{5/2}$, E^{exp}_{em}, and W^{exp}_{em} obtained by the spectral fitting to the experimental spectra in the literature were plot in the panels. Emission energy $\epsilon^{\Delta SCF}_{em}$ and FWHM $w^{\Delta SCF}_{em}$ estimated by using the ΔSCF method are plotted in (a,b), respectively.

of $+2.38 \times 10^{-4}$ eV/K. Compared to the experimental results, the ΔSCF approach not only overestimates the absolute value of the temperature coefficient but also inverts the sign. On the other hand, the ELA method yields the correct sign, while it also overestimates the absolute value. The discrepancy between the experimental and calculated temperature coefficients is attributed to errors in estimating the Franck-Condon shift $E_{FC,g}$ and $E_{FC,e}$. By fitting the curve of Equation (19) to ϵ^{exp}_{em}, noting that $E_{FC,g} + E_{FC,e} = (\Omega_g{}^2 + \Omega_e{}^2)/\ \Delta Q^2 = \Delta S(0)$, $E_{FC,g}$ and $E_{FC,e}$ are found to be 0.122(5) and 0.218(5) eV, respectively, where the experimental $\Delta S(0)$ is 0.34 eV. Also, the curve fitting to ϵ^{cal}_{em} yields $E_{FC,g} = 0.031(80)$ eV and $E_{FC,e} = 0.279(80)$ eV, where $\Delta S(0) =$ 0.31 eV. In the electronic state obtained by DFT calculation, $E_{FC,g}$ and $E_{FC,e}$ are estimated to deviate from the actual values by about 0.1 eV.

The splitting of the high- and low-energy bands due to the SO interaction in Ce $4f^15d^0$ state, $\Delta^{cal}_{SO} = \epsilon^{cal}_{5/2} - \epsilon^{cal}_{7/2}$, is 0.38 eV at 100 K and 0.37 eV at 700 K. These values are 58% overestimated from the experimental values $\Delta^{exp}_{SO} = \epsilon^{exp}_{5/2} - \epsilon^{exp}_{7/2} = 0.24$ eV at 5 K and 0.23 eV at 600 K.

Similar to peak energy, the temperature dependence of the emission peak FWHM has also been estimated using the harmonic oscillator approximation [15–17].

$$w_{em}\ (T) = \sqrt{8 \ln 2}\ \hbar\Omega_g \sqrt{S_g \frac{\Omega_g}{\Omega_e}} \sqrt{\coth \frac{\hbar\Omega_e}{2k_B T}} \qquad (20)$$

Furthermore, at classical limit, $2k_BT > \hbar\Omega_e$, $w_{em}(T)$ is approximated by

$$w_{em}\ (T) \sim \sqrt{8 \ln 2} \frac{\Omega_g}{\Omega_e} \sqrt{2k_B T \hbar \Omega_g S_g} \qquad (21)$$

In Figure 5b, the magenta solid line shows the calculated temperature dependence of $w^{\Delta SCF}_{em}$, and the magenta dotted line shows its classical limit curve. As the agreement of the two curves indicates, the classical limit holds at temperatures above 300 K ($2k_BT = 51.8$ meV $> \hbar\Omega_e = 37.8$ meV). The w^{cal}_{em} of the simulated spectra overlaps with the classical limit curve, indicating that the FPMD spectral accumulation method estimates transition energy fluctuation widths comparable to those obtained by the ΔSCF method. However, in the temperature range from 300 to 700 K, both w^{cal}_{em} and $w^{\Delta SCF}_{em}$ are ~1.6 times larger than w^{exp}_{em}. By fitting the curve of Equation (20) to w^{exp}_{em}, $E_{FC,g}$ and $E_{FC,e}$ are found to be 0.174 and 0.166 eV, respectively. Furthermore, fitting the curve of Equation (21) to w^{cal}_{em} gives $E_{FC,g} = 0.219$ eV and $E_{FC,e} = 0.091$ eV. Thus, like the previous considerations regarding the temperature coefficient of the emission peak energy, the overestimation of w^{cal}_{em} is caused by the overestimation of $E_{FC,g}$ by ~0.1 eV and underestimation of $E_{FC,e}$ by ~0.1 eV compared to the actual values.

As shown in Figure 5c, the calculated intensity ratio $s^{cal}_{7/2}/s^{cal}_{5/2}$ decreases slightly with temperature from 0.54 at 100 K, while the temperature coefficient is negligibly small at $-4.2(7) \times 10^{-5}$ K^{-1}. On the other hand, the ratio $s^{exp}_{7/2}/s^{exp}_{5/2}$ obtained by spectral fitting of observed spectra increases with temperature from 0.46 at 5 K with the relatively large coefficient $+4.2(7) \times 10^{-4}$ K^{-1}. However, as the temperature increases, the two emission bands overlap, making separation by fitting difficult. The intensity ratios tend to be estimated closer to 1 than the true value. Therefore, the actual value of $s^{exp}_{7/2}/s^{exp}_{5/2}$ is thought to be constant at approximately 0.5, such as $s^{exp}_{7/2}/s^{exp}_{5/2}$.

Figure 5d,e shows the temperature dependence of the calculated peak energy E^{cal}_{em} and the FWHM W^{cal}_{em} of the whole emission band consisting of the superposition of the $5d_1 \rightarrow 2F_{7/2}$ and the $5d_1 \rightarrow {}^2F_{5/2}$ bands. At low temperatures where the two emission bands are separated, the E^{cal}_{em} coincides with the peak energy $\epsilon^{cal}_{5/2}$ of the $5d_1 \rightarrow {}^2F_{5/2}$ component. As w^{cal}_{em} increases with increasing temperature, the two bands merge, and the E^{cal}_{em} linearly approaches the midpoint between $\epsilon^{cal}_{5/2}$ and $\epsilon^{cal}_{7/2}$. This behavior is like that of the experimental whole emission band peak energy E^{exp}_{em}, while the E^{cal}_{em} is slightly underestimated at 96% and 93% of the E^{exp}_{em} at 100 and 600 K, respectively. Since zero-point vibrations are not considered, as the temperature is lowered, the FWHM w^{cal}_{em} of each band approaches zero, and the W^{cal}_{em} asymptotes to the $\Delta^{cal}_{SO} = 0.38$ eV. On the other hand, the FWHM W^{exp}_{em} of experimental whole spectrum linearly increased with temperature from 0.37 eV at 5 K, since zero-point motion of atoms

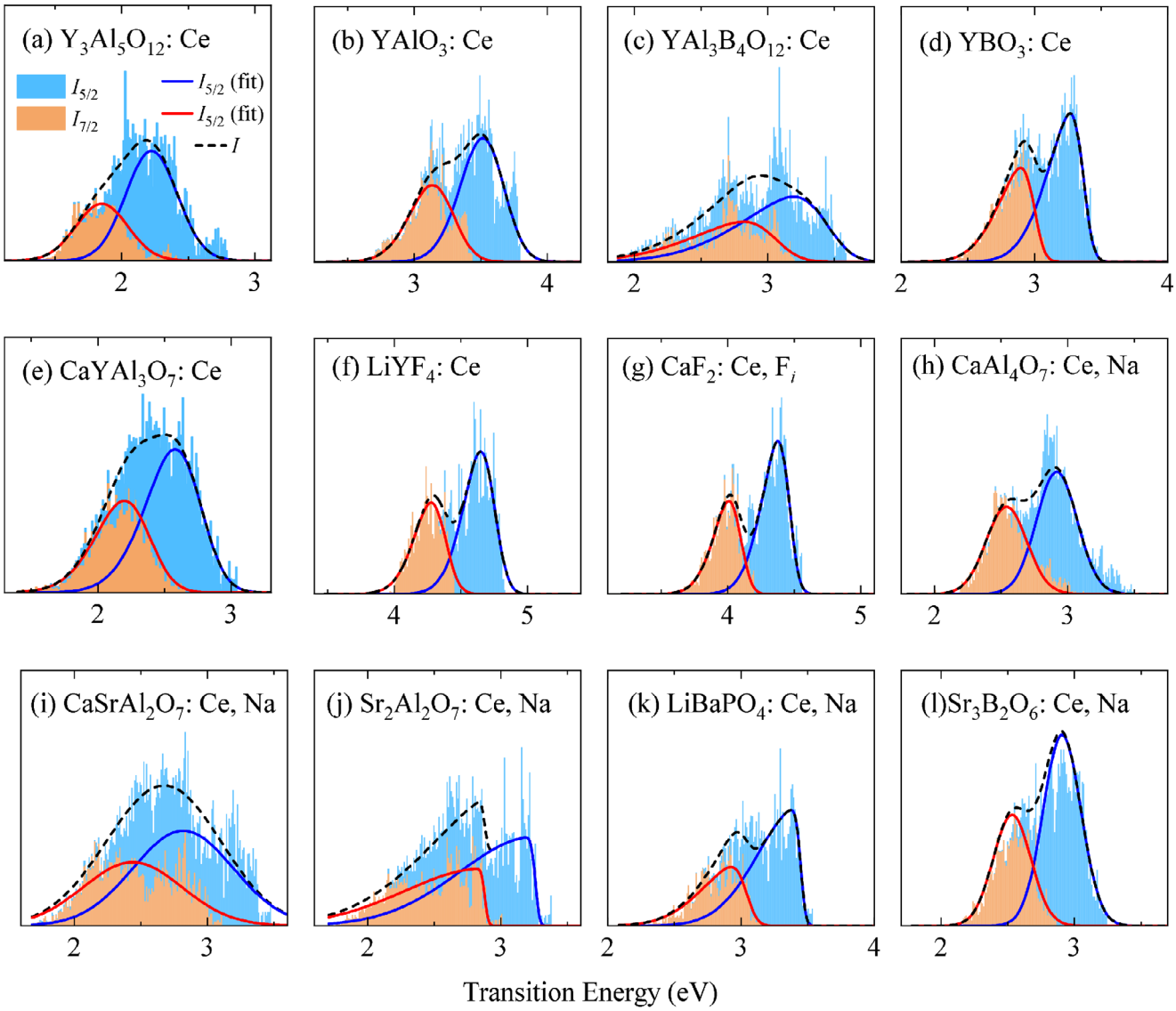

FIGURE 6 | Emission spectra at 300 K calculated by the ELA method for a series of Ce^{3+}-activated phosphors; (a) $Y_3Al_5O_{12}$:Ce, (b) $YAlO_3$:Ce, (c) $YAl_3B_4O_{12}$:Ce, (d) YBO_3:Ce, (e) $CaYAl_3O_7$:Ce, (f) $LiYF_4$:Ce, (g) CaF_2:Ce,F, (h) $CaAl_2O_4$:Ce,Na, (i) $CaSrAl_2O_7$:Ce,Na, (j) $Sr_2Al_2O_7$:Ce,Na, (k) $LiBaPO_4$:Ce,Na, and (l) $Sr_3B_2O_6$:Ce,Na. Light blue and orange parts of stacked bar graphs respectively indicate intensities of $5d_1 \rightarrow {}^2F_{5/2}$ ($I_{5/2}(\epsilon)$) and the $5d_1 \rightarrow {}^2F_{7/2}$ ($I_{7/2}(\epsilon)$) components. Blue and red lines indicate peak fitting curves for $I_{5/2}(\epsilon)$ and $I_{7/2}(\epsilon)$ components, respectively, and the black dashed line indicates the sum of fitting curves.

gives the FWHM $w_{em}^{exp} \sim 0.216$ eV comparable to the SO splitting $\Delta_{so}^{exp} = 0.29$ eV even at 0 K. Above 300 K, W_{em}^{cal} increases linearly at a rate of $2.6(8) \times 10^{-4}$ eV/K, which is close to that of W_{em}^{exp}. The value of W_{em}^{cal} at 300 K is 0.660 eV, 1.54 times larger than the measured value $(1.2(1) \times 10^{-4}$ eV/K).

2.3 | Spectral Calculations for Various Known Ce^{3+}-Activated Phosphors

As shown in Figure 6, the Ce^{3+} $4f^0 5d^1 \rightarrow 4f^1 5d^0$ emission spectra at 300 K were also simulated for the 11 phosphor host systems, including $YAlO_3$ [25], $YAl_3B_4O_{12}$ [26], YBO_3 [26], $CaYAl_3O_7$ [27], $LiYF_4$ [28], CaF_2 [29], $CaAl_4O_7$ [30], $CaSrAl_2SiO_7$ [31], $Sr_2Al_2SiO_7$ [32], $LiBaPO_4$ [33], and $Sr_3B_2O_6$ [34], in addition to YAG listed in Table S1. This table contains the U_{Ce}^{opt} used for structure optimization, total energy, and TDM calculations, along with the parameters obtained by ΔSCF analysis, including $\epsilon_{abs}^{\Delta SCF}(0)$, $\epsilon_{em}^{\Delta SCF}(0)$, $E_{FC,g}$, $E_{FC,e}$, and ΔQ. Additionally, the results of harmonic oscillator model analysis, $\hbar\Omega_g$, $\hbar\Omega_e$, S_g, S_e, the emission peak energy $\epsilon_{em}^{\Delta SCF}(300)$, and FWHM $w_{em}^{\Delta SCF}(300)$ at 300 K are listed in Table S2. By the spectral fitting of skew normal distribution functions to the simulated spectra $I_{5/2}(\epsilon)$ and $I_{7/2}(\epsilon)$ shown in Figure 6, we also obtained $\epsilon_{5/2}^{cal}$, $\epsilon_{7/2}^{cal}$, $w_{5/2}^{cal}$, $w_{7/2}^{cal}$ and $s_{7/2}^{cal}/s_{5/2}^{cal}$ at 300 K listed in Table S3, and E_{em}^{cal} and W_{em}^{cal} listed in Table S4. For comparison, the experimental peak energies E_{em}^{exp} and FWHM W_{em}^{exp} read from spectra at 300 K in the literature, as shown in Figure S5, are also listed in Table S4.

As shown in the $\epsilon_{em}^{\Delta SCF}(300)$ versus $\epsilon_{5/2}^{cal}(300)$ plot in Figure 7a, all data points are distributed around the line of $\epsilon_{5/2}^{cal} = \epsilon_{em}^{\Delta SCF}$.

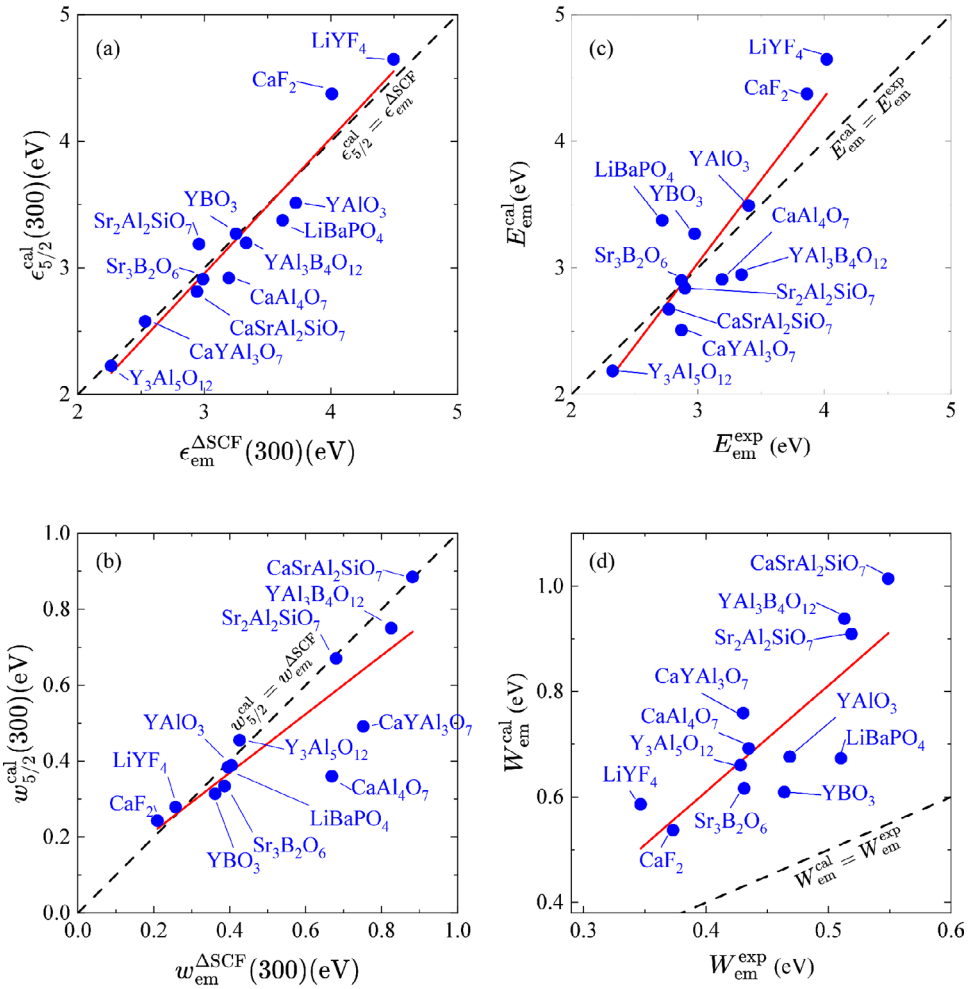

FIGURE 7 | Comparison between the results of ΔSCF analysis and ELA method at 300 K for a series of Ce^{3+}-activated phosphors: (a) Peak energy of $5d_1 \rightarrow {}^2F_{5/2}$ band ($\epsilon_{5/2}^{cal}$) versus ΔSCF emission energy ($\epsilon_{em}^{\Delta SCF}$) (b) FWHM of $5d_1 \rightarrow {}^2F_{5/2}$ emission band ($w_{5/2}^{cal}$) versus ΔSCF FWHM ($w_{em}^{\Delta SCF}$). Comparison between calculated and experimental whole emission spectra at 300 K for a series of Ce^{3+}-activated phosphors: (c) maximum emission energy E_{em}^{cal} versus E_{em}^{exp}, (d) FWHM of emission band W_{em}^{cal} versus W_{em}^{exp}.

The result of the statistical analysis, summarized in Table S5, indicates the $\epsilon_{5/2}^{cal}(300)$ agrees well with $\epsilon_{em}^{\Delta SCF}(300)$ in accuracy within 0.16(11) eV or 5(3)%. This indicates that the total energy difference between the GSEC and ESEC obtained by the ΔSCF approach is nearly identical to the energy difference between the lowest 5d level and the lowest 4f level in the $N-1$ electron calculations. Similarly, as shown in Figure 7b, $w_{em}^{\Delta SCF}(300)$ agrees with $w_{5/2}^{cal}(300)$ in accuracy within 0.07(10) eV or 13(14)%, while $w_{em}^{\Delta SCF}(300)$ in $CaAl_4O_7$:Ce,Na and $CaYAl_3O_7$:Ce systems are exceptionally 1.6 and 1.9 times larger than $w_{5/2}^{cal}(300)$. It implies that the harmonic oscillator approximation for the shape of the ES and GS energy surface is not valid in these systems, resulting in the overestimation of the line broadening. The FPMD spectra accumulation method generally provides results that are consistent with the ΔSCF method in calculating the peak energy and FWHM of the emission bands and may also provide more accurate predictions for the FWHM in anharmonic systems.

Figure 7c shows the peak energies of the calculated total emission spectra E_{em}^{cal} versus the experimental values E_{em}^{exp} read from the literature spectra shown in Figure S5. The data points are distributed around the line of $E_{em}^{cal} = E_{em}^{exp}$, and the statistical analysis and linear fitting results are summarized in Table S6, indicating E_{em}^{cal} coinciding with E_{em}^{exp} to within 0.30(22) eV or 9(6)%.

Figure 7d shows the calculated FWHM of the total emission spectra W_{em}^{cal} versus the experimental values W_{em}^{exp}. Each data point is located at a position significantly different from the line of $W_{em}^{cal} = W_{em}^{exp}$, and according to the statistical data shown in Table S6, W_{em}^{cal} is overestimated by approximately 1.6 times compared to W_{em}^{exp}. As shown in Figure S6, W_{em}^{cal} has a linear relationship with w_{em}^{cal}, $W_{em}^{cal} - \Delta_{SO}^{cal} = 0.75(2)w_{em}^{cal}$, using the almost system-independent SO splitting Δ_{SO}^{cal} of 0.38(2) eV. Assuming this relationship is valid for experimental data, i.e., $W_{em}^{exp} - \Delta_{SO}^{exp} = 0.75(2)w_{em}^{exp}$ holds under $\Delta_{SO}^{exp} = 0.29$ eV, we can see how much w_{em}^{cal} is overestimated compared to w_{em}^{exp} by comparing $W_{em}^{exp} - \Delta_{SO}^{exp}$ and $W_{em}^{cal} - \Delta_{SO}^{cal}$. The statistical data for $W_{em}^{cal} - \Delta_{SO}^{cal}$ shown in Table S6 indicate $w_{em}^{cal} = 2.2(6)w_{em}^{exp}$. Since w_{em}^{cal} and $w_{em}^{\Delta SCF}$ are approximately equal in most systems, $w_{em}^{\Delta SCF}$ is also overestimate by about 2 compared to w_{em}^{exp}. The extent of overestimation is the same as that suggested when discussing the temperature dependence of the FWHM for YAG:Ce in the previous section. In all the systems, the DFT calculations are thought to overestimate $E_{FC,g}$ and underestimate

$E_{FC.e}$ relative to the measurements by about 0.1 eV. For a series of Ce^{3+}-activated systems, DFT calculations appear to overestimate $E_{FC.g}$ and underestimate $E_{FC.g}$ by about 0.1 eV compared to the actual values.

3 | Conclusions

By conducting SCF calculations with the $N-1$ electron configuration on the crystal structure models of the Ce^{3+}-activated system, the KSO eigenvalues and wavefunctions were obtained, providing transition energies and probabilities for the $4f^0 5d^1 \rightarrow 4f^1 5d^0$ transition that align with experimental emission energies and many-body calculation results in the literature. Applying this calculation method to each snapshot of the FPMD performed with ESEC allowed us to analyze the time evolution of transition energies and probabilities. As a result of ELA along the MD trajectory, we derived emission spectra similar to the experimental spectra, showing the SO splitting and peak broadening caused by atomic thermal motion.

The emission peak energy and emission FWHM caused by atomic thermal motion calculated by the ELA method align with those from the ΔSCF method above 300 K. However, the temperature coefficient of peak energy is roughly ten times higher than the experimental value. The peak energies of all emission bands at 300 K obtained via the ELA method match the measured peak energies within a 9(7)% error margin, while the FWHMs of these bands at 300 K are 158(19)% of the measured values. This overestimation results from the calculated SO splitting and thermal FWHM being 130% and 223(65)% of the actual values, respectively. The latter is likely because the Franck-Condon shifts of the ground and excited states from DFT calculations are over- and underestimated by about 0.1 eV, respectively.

By considering the systematic error between the predicted and measured values, this calculation method can be used to predict the luminescence properties of new candidate phosphor compounds.

4 | Computational Methods

4.1 | SCF and Structure Optimization Calculations

This study's DFT and FPMD calculations were carried out using the Vienna ab initio simulation package (VASP) [35–38]. The electronic structure of the periodic boundary system was determined using the projector-augmented-wave (PAW) method with the revised Perdew–Burke–Ernzerhof (PBEsol) correlation-exchange functional [39]. The high-energy cutoff of the plane wave basis, the energy threshold for SCF convergence, and the atomic force threshold for structure optimization were set to 500 eV, 1×10^{-7} eV, and 5×10^{-3} eV, respectively. The k-mesh density d_k used for Brillouin zone (BZ) integration was 5.0 Å. For example, a k-mesh of $2\pi d_k/a \times 2\pi d_k/a \times 2\pi d_k/a \sim 3 \times 3 \times 3$ was used for a cubic system with the lattice parameter $a = 12$ Å. The contributions of the Ce 4f and Ce 5d orbitals to each KSO are evaluated by $(\Sigma_m C_{Ce,2,m} - \Sigma_m C_{Ce,3,m}) / \Sigma_{m l\alpha} C_{\alpha l m}$, where $C_{Ce,2,m}$ ($m = -2, -1, \ldots, 2$) and $C_{Ce,3,m}$ ($m = -3, -2, \ldots, 3$) are the Ce d- and Ce f-projected wavefunction characters, and $C_{\alpha l m}$ is the spdf- and site-projected character for atom index α, and the angular moment and magnetic quantum numbers, l (= 0, 1, …, 3) and m (= $-l$, $-l$ +1, …, l). When the KSO is composed mainly of Ce 4f orbitals, the value will be close to −1, and when it is composed primarily of Ce 5d orbitals, it will be close to +1.

4.2 | Construction of Structural Models of Ce^{3+}-Activated Phosphors

As calculation targets, we chose twelve known phosphor systems containing only one crystallographic site of Y, La, or alkaline earth metal elements (Ca, Sr, and Ba) that Ce can substitute. After optimizing the primitive cell structure of the host compound, it was expanded into a supercell containing about 100 atoms, and one of the Y, La, or alkaline earth sites was substituted by Ce. When an alkaline earth site with a formal charge of +2 was substituted, the nearest alkaline earth site was substituted by Na with a charge of +1, preserving the +3 charge of Ce. The geometry of the Ce-substituted model was optimized using non-spin-polarized calculations with a pseudopotential (PP) for Ce, treating the 4f states as core levels.

4.3 | Determination of On-Site Coulomb Parameter on Ce Sites

The subsequent DFT calculations were performed using the PP for Ce, treating the 4f states as valence levels and an effective on-site Coulomb interaction ($+U$) at the Ce site (U_{Ce}). To determine an appropriate value of U_{Ce} ($U_{Ce}{}^{opt}$) such that the position of the occupied Ce 4f level in the band gap satisfies the results of spectroscopic experiments, we used the procedure referring to the result of SCF calculation using Heyd–Scuseria–Ernzerhof (HSE06) hybrid functional calculation. Although HSE06 calculations are more expensive than PBEsol+U calculations, they are known to yield Ce 4f positions consistent with experimental absorption and emission data, without the need for the $+U$ approach [40–42]. By performing the Γ-point-only spin-polarized SCF calculations with U_{Ce} ranging from 0 to 9 eV, we obtained the KSO energies as a function of U_{Ce} as shown in Figure S7. The energies of the lowest Ce 4f orbital (ϵ_{Ce4f}) vary with U_{Ce} between the valence band maximum (ϵ_{VBM}) and the conduction band minimum (ϵ_{CBM}). Here, the ratio r of the energy difference between the lowest 4f level and the VBM ($\epsilon_{Ce4f} - \epsilon_{VBM}$) to the band gap ($\epsilon_{CBM} - \epsilon_{VBM}$) is defined as a function of U_{Ce}: $r(U_{Ce}) = [\epsilon_{Ce4f}(U_{Ce}) - \epsilon_{VBM}] / [\epsilon_{CBM} - \epsilon_{VBM}]$. The SCF calculation using the HSE06 without $+U$ was also performed for the same crystal structure model and obtained the reference ratio r_{HSE}. By fitting a linear function to the r versus U_{Ce} plot, the $U_{Ce}{}^{opt}$ was determined such that $r(U_{Ce}{}^{opt}) = r_{HSE}$. Figure S8a shows the KSO energy at the Γ point for the $A_e{}^{-1}$ state in the YAG:Ce system as a function of U_{Ce}. The $5d_1 \rightarrow {}^2F_{5/2}$ and $5d_1 \rightarrow {}^2F_{7/2}$ transition energies, calculated from the energy differences between these levels, decrease linearly with U_{Ce} (Figure S8b). When U_{Ce} changes by 1 eV from the optimal value $U_{Ce}{}^{opt}$, the emission energy changes by approximately 0.16 eV. Therefore, to predict the emission energy with an accuracy of ±0.1 eV (±10 nm at a wavelength of 500 nm), U_{Ce} must be optimized to within ±0.6 eV.

4.4 | TDM Calculation

The VASPBandUnfolding code was used to convert the pseudo-wavefunctions φ_i^{PS} generated by VASP into all-electron wavefunctions φ and calculate the transition dipole moments from them [43].

4.5 | FPMD Calculation

All FPMD runs in this study were performed with a timestep of 1 fs and the ESEC. The ES relaxed structures $\mathbf{Q}_e$ were subjected to an equilibration run of 257 fs in the NVT (fixed number of atoms, volume, and temperature) ensemble using a Nose-Hoover thermostat with a convergence temperature ranging from 100 to 700 K. The production runs, which lasted 1025 fs to collect the trajectory, were performed in the NVE (fixed number of atoms, volume, and total energy) ensemble.

Author Contributions

Satoru Matsuishi, **Yukinori Koyama**, and **Takashi Takeda** devised the basic idea of this study. **Satoru Matsuishi** conducted calculations under the guidance of **Yukinori Koyama** and **Hidekazu Ikeno**, and **Takashi Takeda** contributed to the selection of calculation targets. **Satoru Matsuishi** prepared the original draft of the manuscript. All the authors approved the final version of the manuscript.

Acknowledgements

This work was supported by the Japan Science and Technology Agency (JST), CREST Grant Number JPMJCR19J2. The calculations in this study were performed on the Numerical Materials Simulator at the National Institute for Materials Science (NIMS).

Funding

This work was supported by the Japan Science and Technology Agency (JST), CREST Grant Number JPMJCR19J2.

Conflicts of Interest

The authors declare no conflicts of interest.

Data Availability Statement

The data that support the findings of this study are available in the supplementary material of this article.

References

1. K. Morimoto, H. Kasugai, T. Takizawa, et al., "60.2: Distinguished Paper:a 30 W Pure Blue Emission with NUV Laser-Diode-Pumped Phosphor for High-Brightness Projectors," *SID Symposium Digest of Technical Papers* 44 (2013): 832–835, https://doi.org/10.1002/j.2168-0159.2013.tb06346.x.

2. Y. H. Song, E. K. Ji, B. W. Jeong, M. K. Jung, E. Y. Kim, and D. H. Yoon, "High Power Laser-driven Ceramic Phosphor Plate for Outstanding Efficient White Light Conversion in Application of Automotive Lighting," *Scientific Reports* 6 (2016): 31206, https://doi.org/10.1038/srep31206.

3. A. Lenef, M. Raukas, J. Wang, and C. Li, "Phosphor Performance under High Intensity Excitation by InGaN Laser Diodes," *ECS Journal of Solid State Science and Technology* 9 (2020): 016019, https://doi.org/10.1149/2.0352001JSS.

4. K. A. Denault, M. Cantore, S. Nakamura, S. P. DenBaars, and R. Seshadri, "Efficient and Stable Laser-Driven White Lighting," *AIP Advances* 3 (2013): 072107, https://doi.org/10.1063/1.4813837.

5. "4K HDR Movies with BT.2020 Color beyond DCI-P3", Rec. ITU-R BT.2020, Ed., accessed 2012, https://www.avsforum.com/threads/4k-hdr-movies-with-bt-2020-color-beyond-dci-p3.3256461/.

6. Y. Zhuo, A. Mansouri Tehrani, A. O. Oliynyk, A. C. Duke, and J. Brgoch, "Identifying an Efficient, Thermally Robust Inorganic Phosphor Host via Machine Learning," *Nature Communications* 9 (2018): 4377, https://doi.org/10.1038/s41467-018-06625-z.

7. S. Behara, S. Rath, and T. Thomas, "Machine Learning (ML) as a Tool for Phosphor Design: A Perspective," *Materials Letters* 308 (2022): 131061, https://doi.org/10.1016/j.matlet.2021.131061.

8. Y. Koyama, H. Ikeno, M. Harada, S. Funahashi, T. Takeda, and N. Hirosaki, "Rapid Discovery of New Eu^{2+}-Activated Phosphors with a Designed Luminescence Color Using a Data-driven Approach"," *Materials Advance* 4 (2023): 231, https://doi.org/10.1039/D2MA00881E.

9. J. Gracia, L. Seijo, Z. Barandiarán, D. Curulla, H. Niemansverdriet, and W. Van Gennip, "Ab Initio Calculations on the Local Structure and the 4f–5d Absorption and Emission Spectra of -doped YAG"," *Journal of Luminescence* 128 (2008): 1248, https://doi.org/10.1016/j.jlumin.2007.12.027.

10. L. Ning, C. Wu, L. Li, et al., "First-Principles Study on Structural Properties and 4f → 5d Transitions of Locally Charge-Compensated Ce^{3+} in CaF_2"," *Journal of Physical Chemistry C* 116 (2012): 18419, https://doi.org/10.1021/jp305593h.

11. L. Seijo and Z. Barandiarán, "4f and 5d Levels of Ce^{3+} in D_2 8-fold Oxygen Coordination"," *Optical Materials* 35 (2013): 1932, https://doi.org/10.1016/j.optmat.2012.12.007.

12. L. Seijo and Z. Barandiarán, "Large Splittings of the 4f Shell of Ce^{3+} in Garnets"," *Physical Chemistry Chemical Physics* 16 (2014): 3830, https://doi.org/10.1039/C3CP53549E.

13. Y. Jia, A. Miglio, S. Poncé, X. Gonze, and M. Mikami, "First-Principles Study of Ce^{3+}-Doped Lanthanum Silicate Nitride Phosphors: Neutral Excitation, Stokes Shift, and Luminescent Center Identification, Stokes Shift, and Luminescent Center Identification," *Physical Review B* 93 (2016): 155111, https://doi.org/10.1103/PhysRevB.93.155111.

14. Y. Jia, S. Poncé, A. Miglio, M. Mikami, and X. Gonze, "Assessment of First-Principles and Semiempirical Methodologies for Absorption and Emission Energies of Ce^{3+}-Doped Luminescent Materials"," *Advanced Optical Materials* 5 (2017): 1600997, https://doi.org/10.1002/adom.201600997.

15. Y. Jia, A. Miglio, S. Poncé, M. Mikami, and X. Gonze, "First-principles Study of the Luminescence of Eu^{2+}-doped Phosphors"," *Physical Review B* 96 (2017): 125132, https://doi.org/10.1103/PhysRevB.96.125132.

16. J. Bouquiaux, S. Poncé, Y. Jia, A. Miglio, M. Mikami, and X. Gonze, "Importance of Long-Range Channel Sr Displacements for the Narrow Emission in $Sr[Li_2Al_2O_2N_2]:Eu^{2+}$ Phosphor"," *Advanced Optical Materials* 9 (2021): 2100649, https://doi.org/10.1002/adom.202100649.

17. (eds.: R.-S. Liu and X.-J. Wang), *Phosphor Handbook Fundamentals of Luminescence* (CRC Press, 2022), https://doi.org/10.1201/9781003098690.

18. Y. Han, D. J. Vogel, T. M. Inerbaev, P. S. May, M. T. Berry, and D. S. Kilin, "Photoinduced Dynamics to Photoluminescence in Ln^{3+} (Ln = Ce, Pr) Doped β-$NaYF_4$ Nanocrystals Computed in Basis of Non-collinear Spin DFT with Spin-orbit Coupling," *Molecular Physics* 116 (2018): 697–707, https://doi.org/10.1080/00268976.2017.1416193.

19. T. M. Inerbaev, Y. Han, T. B. Bekker, and D. S. Kilin, "Photoluminescence in Cerium-Doped Fluoride Borate Crystals," *The Journal of Physical Chemistry C* 127 (2023): 9213–9224, https://doi.org/10.1021/acs.jpcc.2c08711.

20. H. Przybylińska, C.-G. Ma, M. G. Brik, et al., "Electronic Structure of Ce^{3+} Multicenters in Yttrium Aluminum Garnets"," *Applied Physics Letters* 102 (2013): 241112, https://doi.org/10.1063/1.4812190.

21. V. Bachmann, C. Ronda, and A. Meijerink, "Temperature Quenching of Yellow Ce^{3+} Luminescence in YAG:Ce"," *Chemistry of Materials* 21 (2009): 2077–2084, https://doi.org/10.1021/cm8030768.

22. J. F. Janak, "Proof That $\partial E/\partial n_i = \epsilon$ in Density-functional Theory"," *Physical Review B* 18 (1978): 7165, https://doi.org/10.1103/PhysRevB.18.7165.

23. S. Steiner, S. Khmelevskyi, M. Marsmann, and G. Kresse, "Calculation of the Magnetic Anisotropy with Projected-augmented-wave Methodology and the Case Study of Disordered $Fe_{1-x}Co_x$ Alloys"," *Physical Review B* 93 (2016): 224425, https://doi.org/10.1103/PhysRevB.93.224425.

24. L.-J. Lyu and D. S. Hamilton, "Radiative and Nonradiative Relaxation Measurements in Ce^{3+} Doped Crystals," *Journal of Luminescence* 48–49 (1991): 251, https://doi.org/10.1016/0022-2313(91)90116-D.

25. T. Tomiki, H. Ishikawa, T. Tashiro, et al., "Ce^{3+} Centres in $YAlO_3$ (YAP) Single Crystals," *Journal of the Physical Society of Japan* 64 (1995): 4442–4449, https://doi.org/10.1143/JPSJ.64.4442.

26. A. Bril, G. Blasse, and J. A. De Poorter, "Fast-Decay Phosphors," *Journal of The Electrochemical Society* 117 (1970): 346, https://doi.org/10.1149/1.2407508.

27. Y.-K. Choi, P. Halappa, C. Shivakumara, V. Dubey, and V. Singh, "Blue Emitting Ce^{3+}-doped $CaYAl_3O_7$ Phosphors Prepared by Combustion Route"," *Optik* 181 (2019): 1113, https://doi.org/10.1016/j.ijleo.2018.10.213.

28. Y. Yokota, T. Yanagida, K. J. Kim, et al., "Growth, Optical Properties and Neutron Responses of Ce^{3+} Doped LiYF4 Single Crystals," in 2008 IEEE Nuclear Science Symposium Conference Record (IEEE, 2008), 1236–1239, https://doi.org/10.1109/NSSMIC.2008.4774629.

29. M. Uy, K. Shinohara, M. J. F. Empizo, et al., "Evidence of Undistorted 8-Coordinated Cubic (O_h) Ce^{3+} Center in Moderately-Doped (0.01 mol %) CaF_2 Single Crystal"," *Journal of the Physical Society of Japan* 91 (2022): 124713, https://doi.org/10.7566/JPSJ.91.124713.

30. D. Jia, R. S. Meltzer, W. M. Yen, W. Jia, and X. Wang, "Green Phosphorescence of $CaAl_2O_4$:Tb^{3+},Ce^{3+} through Persistence Energy Transfer," *Applied Physics Letters* 80 (2002): 1535–1537, https://doi.org/10.1063/1.1456955.

31. S. Miao, Z. Xia, M. S. Molokeev, J. Zhang, and Q. Liu, "Crystal Structure Refinement and Luminescence Properties of Blue-green-emitting $CaSrAl_2SiO_7$:Ce^{3+},Li^+,Eu^{2+} Phosphors"," *Journal of Materials Chemistry C* 3 (2015): 8322, https://doi.org/10.1039/C5TC01629K.

32. T. Richhariya, N. Brahme, D. P. Bisen, Y. Patle, E. Chandrawanshi, and N. Shah, "Luminescence Properties of Blue-emitting Ce^{3+}-doped Series of $Ca_2Al_2SiO_7$ and $Sr_2Al_2SiO_7$ Phosphors"," *Journal of Materials Science—Materials in Electronics* 32 (2021): 20793, https://doi.org/10.1007/s10854-021-06593-z.

33. D. Wei, Y. Huang, S. Zhang, Y. M. Yu, and H. J. Seo, "Luminescence Spectroscopy of Ce^{3+}-doped $ABaPO_4$ (A = Li, Na, K) Phosphors," *Applied Physics B* 108 (2012): 447–453, https://doi.org/10.1007/s00340-012-4969-x.

34. X. Li, C. Liu, L. Guan, et al., "An Ideal Blue $Sr_3B_2O_6$: Ce^{3+} Phosphor Prepared by Sol-combustion Method"," *Materials Letters* 87 (2012): 121, https://doi.org/10.1016/j.matlet.2012.07.094.

35. G. Kresse and J. Hafner, "Ab Initio Molecular Dynamics for Liquid Metals," *Physical Review B* 47 (1993): 558–561, https://doi.org/10.1103/PhysRevB.47.558.

36. G. Kresse and J. Furthmüller, "Efficiency of Ab-initio Total Energy Calculations for Metals and Semiconductors Using a Plane-wave Basis Set," *Computational Materials Science* 6 (1996): 15–50, https://doi.org/10.1016/0927-0256(96)00008-0.

37. G. Kresse and J. Furthmüller, "Efficient Iterative Schemes for Ab Initio Total-energy Calculations Using a Plane-wave Basis Set," *Physical Review B* 54 (1996): 11169–11186, https://doi.org/10.1103/PhysRevB.54.11169.

38. G. Kresse and D. Joubert, "From Ultrasoft Pseudopotentials to the Projector Augmented-wave Method," *Physical Review B* 59 (1999): 1758–1775, https://doi.org/10.1103/PhysRevB.59.1758.

39. J. P. Perdew, A. Ruzsinszky, G. I. Csonka, et al., "Restoring the Density-Gradient Expansion for Exchange in Solids and Surfaces," *Physical Review Letters* 100 (2008): 136406, https://doi.org/10.1103/PhysRevLett.100.136406.

40. J. Heyd, G. E. Scuseria, and M. Ernzerhof, "Hybrid Functionals Based on a Screened Coulomb Potential," *The Journal of Chemical Physics* 118 (2003): 8207–8215, https://doi.org/10.1063/1.1564060.

41. S. Li, Y. Li, M. Bäumer, and L. V. Moskaleva, "Assessment of PBE+U and HSE06 Methods and Determination of Optimal Parameter U for the Structural and Energetic Properties of Rare Earth Oxides," *The Journal of Chemical Physics* 153 (2020): 164710, https://doi.org/10.1063/5.0024499.

42. T. Wu, H. Hua, J. Ueda, S. Tanabe, and S. Matsuishi, "Pressure-dependent Photoluminescence of Eu-Activated Aluminate Hydride $Sr_{3-x}A_xAlO_4H$:Eu^{2+} (A = Ca, Ba; x = 0, 1): Application of Advanced U -determination Technique for Luminescence Wavelength Prediction," *Journal of Applied Physics* 132 (2022): 083104, https://doi.org/10.1063/5.0102219.

43. Q. Zheng, VaspBandUnfolding, https://github.com/QijingZheng/VaspBandUnfolding (accessed: 2024).

Supporting Information

Additional supporting information can be found online in the Supporting Information section.

Supporting File: adts70428-sup-0001-SuppMat.pdf.